IEEE Robotics and Automation Letters (RA-L) paper, presented at ICRA 2026, Vienna, Austria. Cite as RA-L paper.

Adaptive Robust Control for Rotation Tracking of a Soft Rotary Actuator with Hysteresis Compensation

Young Min Lee[1,2], Yeoil Yun[1], Hyungpil Moon[1], Hyouk Ryeol Choi[1], Yong Seok Ihn[2] and Ja Choon Koo[1]

***Abstract*—Precise control of soft pneumatic actuators is impeded by significant nonlinearities, particularly large internal volume variations during actuation—a factor often overlooked in conventional modeling. This paper proposes an adaptive robust control (ARC) framework designed for high-performance, energy-efficient control of soft actuators with non-negligible volume dynamics. The framework integrates a Modified Prandtl-Ishlinskii (MPI) model for hysteresis compensation with a real-time volume estimator using an internal Time-of-Flight (ToF) sensor. The ARC law then systematically handles uncertainties from both valve parameter variations and the volume estimation process. Experimental validation, through direct comparison with a conventional fixed-volume model, demonstrates that this volume-aware approach achieves robust trajectory tracking with significantly reduced control effort and energy consumption. This work establishes that explicitly modeling internal volume dynamics is crucial for developing high-performance control systems for a broad class of soft pneumatic actuators.**

***Index Terms*—Soft Pneumatic Actuators, Volume Modeling, Hysteresis, Adaptive Robust Control, On/off Valves**

I. INTRODUCTION

SOFT pneumatic actuators (SPAs) are pivotal in modern robotics, offering compliance for various applications [1]–[7]. However, their precise control is challenging due to inherent nonlinearities and model uncertainties [8]–[10]. Hysteresis is often addressed using models like the Prandtl-Ishlinskii (PI) [10], [11], while uncertainties are managed by robust strategies such as Sliding Mode Control (SMC) [9], [12], [13] and Adaptive Robust Control (ARC) [11], [14], [15]. These robust control methods have also been effectively applied to systems with on-off solenoid valves [16]. A critical, often-simplified factor is the actuator's internal volume variation [8], [17]. While many studies assume this volume change is negligible [18], for actuators with large deformations, this assumption becomes a primary source of unmodeled dynamics and energy inefficiency [5], [12], [19].

A framework that explicitly measures and integrates real-time volume dynamics into a model-based adaptive robust controller remains an underexplored area [20], [21]. This paper addresses this gap by proposing a universal ARC framework for SPAs with significant volume dynamics. The framework uniquely integrates real-time volume estimation via an internal Time-of-Flight (ToF) sensor, hysteresis compensation with a Modified Prandtl-Ishlinskii (MPI) model, and a robust control law to handle coupled uncertainties. Through experimental validation, we demonstrate that this volume-aware approach achieves robust tracking and improved energy efficiency compared to a conventional fixed-volume model. The presented methodology serves as a generalizable guideline for high-performance control of soft actuators where volume change is a critical dynamic factor.

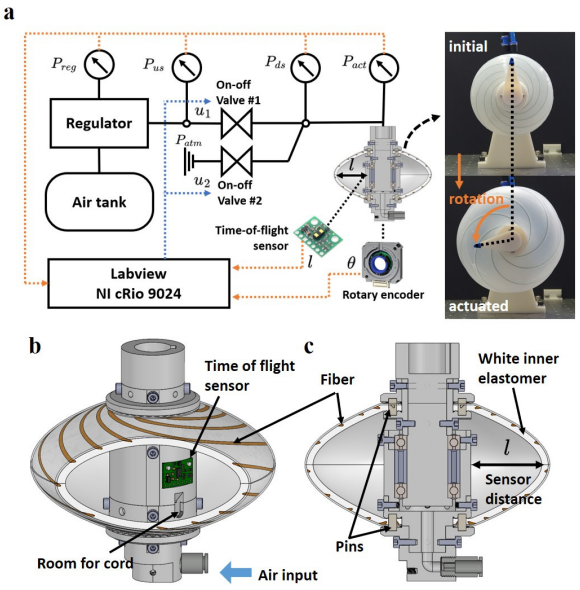

Fig. 1. System overview and actuator design. (a) Schematic of the control system, including pneumatic components, sensors, and the soft rotary actuator in its initial and actuated states. (b) Cutaway view illustrating the internal placement of the ToF sensor. (c) Cross-section view detailing the internal components and the distance (l) measured by the ToF sensor.

II. PROBLEM DEFINITION

The primary objective of this paper is to develop a universal control framework applicable to a broad class of soft pneumatic actuators characterized by significant internal volume variations. Such actuators, while compliant, present considerable control challenges as their pressure dynamics are intrinsically coupled with their changing geometry. To develop and validate this framework, this study focuses on a challenging case study: a soft pneumatic rotary actuator, as shown in Fig. 1. The proposed framework integrates key modules, including a model for pneumatic valve dynamics, a compensator for the actuator's inherent hysteresis, and a state

Manuscript received May 19, 2025; Revised September 30, 2025; Accepted December 3, 2025.

This paper was recommended for publication by Editor Yong-Lae Park upon evaluation of the Associate Editor and Reviewers' comments.

The authors are with [1]the Faculty of Mechanical Engineering, Sungkyunkwan University, Suwon 16419, Republic of Korea, and also with [2]the Korea Institute of Science and Technology (KIST), Seoul 02792, Republic of Korea (Corresponding author: Ja Choon Koo, e-mail: jckoo@skku.edu)

IEEE Robotics and Automation Letters (RA-L) paper, presented at ICRA 2026, Vienna, Austria. Cite as RA-L paper.

estimator for the internal volume dynamics using a ToF sensor. These elements constitute the testbed for demonstrating the efficacy of our universal control approach.

III. Method

A. Pressure dynamics through an On-Off Valve

According to the ISO-6358 standard, the mass flow rate Q_m through an on-off valve is determined by the following parameters:

$$Q_m = \rho_0 C \sqrt{\frac{T_0}{T}} P_u f(P_u, P_d, \sigma_{cr}) \tag{1a}$$

$$f(P_u, P_d, \sigma_{cr}) = \begin{cases} 1 & \text{if } P_d/P_u \leq \sigma_{cr} \\ \sqrt{1 - (\frac{P_d/P_u - \sigma_{cr}}{1-\sigma_{cr}})^2} & \text{if } P_d/P_u > \sigma_{cr}. \end{cases} \tag{1b}$$

Here, C and σ_{cr} represent the sonic conductance and critical ratio, respectively. The valve's conductance, $C(u)$, is linearly related to the PWM input u through experimentally determined coefficients K_{c1} and K_{c0}, which enables energy-efficient and precise flow modulation.

$$C(u) = K_{c1} u - K_{c0} \tag{2}$$

Assuming the actuator's internal air volume V_a changes and the thermodynamic process is adiabatic, the pressure dynamics inside the actuator can be described as:

$$\dot{P} = k \frac{R}{V_a} (Q_{m,1} T_{in} - Q_{m,2} T_{out}) - k \frac{P \dot{V_a}}{V_a} \tag{3}$$

Here, $Q_{m,1}$ and $Q_{m,2}$ denote the mass flow rates, which are determined by the PWM inputs u_1, u_2 for the charging and exhausting valves, respectively.

$$Q_{m,1} = \rho_0 C(u_1) P_{reg} f(P_{reg}, P, \sigma_{cr}) \tag{4a}$$

$$Q_{m,2} = \rho_0 C(u_2) P f(P, P_{atm}, \sigma_{cr}) \tag{4b}$$

B. Hysteresis Modeling

Hysteresis exhibits strong nonlinearity, necessitating accurate modeling techniques. Among these, the PI model is notable for its effective representation of hysteresis through Play operators and the derivation of its inverse model. The Play operator, $H_r(x, y_0, r_h)$, operates as follows:

$$\begin{aligned} y(t) &= H_r(x, y_0, r_h) \\ &= max\{x(t) - r_h, min\{x(t) + r_h, y(t-T)\}\}, \end{aligned} \tag{5a}$$

$$\begin{aligned} y(t=0) &= H_r(x_0, y_0, r_h) \\ &= max\{x(0) - r_h, min\{x(0) + r_h, y(0)\}\} \end{aligned} \tag{5b}$$

where x, y are input and output, t, T are time and sampling period. While the initial model utilized a single hysteresis threshold r_h, it can be expanded to include multiple thresholds and corresponding weights by allowing vector form. This allows the model to be redefined with a more complex structure, as follows:

$$y(t) = \boldsymbol{w_h}^T \boldsymbol{H_r}(x, y_0, \boldsymbol{r_H}) \tag{6}$$

where $\boldsymbol{H_r}(x, y_0, \boldsymbol{r_H}) = [H_r(x, y_0, r_{h0}),\ H_r(x, y_0, r_{h1}),\ ...,\ H_r(x, y_0, r_{h(n-1)})]^T$ holds with $\boldsymbol{w_h} = [w_{h0},\ w_{h1},\ ...,\ w_{h(n-1)}]^T$, $\boldsymbol{r_h} = [r_{h0}, r_{h1}, ..., r_{h(n-1)}]^T$. And also components of the thresholds comply with $0 = r_{h0} < r_{h1} < ... < r_{h(n-1)}$ while weight components can be negative or positive.

The deadzone operator, $D(y, d)$, creates a non-responsive or "dead" zone around the origin of the input-output curve, defined as:

$$D_d(y(t), d) = \begin{cases} y(t) & \text{if } d = 0 \\ max\{y(t) - d, 0\} & \text{if } d > 0 \end{cases} \tag{7}$$

where y is the input and d defines the deadzone width. This operator nullifies output within a specified input range, simulating a threshold for system response. The MPI model integrates the deadzone operator to account for asymmetric hysteresis:

$$z(t) = \boldsymbol{w_d}^T \boldsymbol{D_d}(y, \boldsymbol{d}) \tag{8}$$

where $\boldsymbol{D_d}(y, \boldsymbol{d}) = [D_d(y, d_1), D(y, d_2), ..., D_d(y, d_{m-1})]^T$ holds with $\boldsymbol{w_d} = [w_{d0},\ w_{d1},...,\ w_{d(m-1)}]^T$, $\boldsymbol{d} = [d_0, d_1, ..., d_{(n-1)}]^T$. And also components of the thresholds $0 = r_{h0} < r_{h1} < ... < r_{h(n-1)}$ satisfy as same as the play operator case. The output $z(t)$ represents the final hysteresis output through the play operator and the deadzone operator with input of $x(t)$ and y_0.

The inverse MPI model , $\Psi^{-1}(z(t), \boldsymbol{y'_0}, t)$, shares a similar form with the forward hysteresis model, $\Psi(x(t), y_0, t)$:

$$\begin{aligned} z(t) &= \Psi(x(t), y_0, t) \\ &= \boldsymbol{w_d}^T \boldsymbol{D_d}(\boldsymbol{w_h}^T \boldsymbol{H_r}(x, y_0, \boldsymbol{r_h}), \boldsymbol{d}) \end{aligned} \tag{9a}$$

$$\begin{aligned} x(t) &= \Psi^{-1}(z(t), \boldsymbol{y'_0}, t) \\ &= \boldsymbol{w'_h}^T \boldsymbol{H_{r'}}(\boldsymbol{w'_d}^T \boldsymbol{D_{d'}}(z(t)), \boldsymbol{y'_0}) \end{aligned} \tag{9b}$$

where parameters corresponding inverse MPI operators are established as (25) in Appendix. A

The MPI model's structure allows for the construction of an inverse model, which is essential for the feedforward control path. As shown in Fig.2, an experiment was conducted to identify the model parameters by generating a desired pressure trajectory and fitting the measured rotation data using an optimization tool. The results confirmed a good fit, with a Root Mean Square Error (RMSE) of 0.7399 degrees. This identified forward model can then be used to derive the inverse model parameters for the controller.

C. Volume Estimating Modeling

To control the actuator, its internal volume dynamics, V_a and $\dot{V_a}$, must be explicitly modeled due to significant volume changes. The ToF sensor is placed inside the actuator to measure the distance l to the outer circumference, enabling real-time volume estimation. This relationship was determined

IEEE Robotics and Automation Letters (RA-L) paper, presented at ICRA 2026, Vienna, Austria. Cite as RA-L paper.

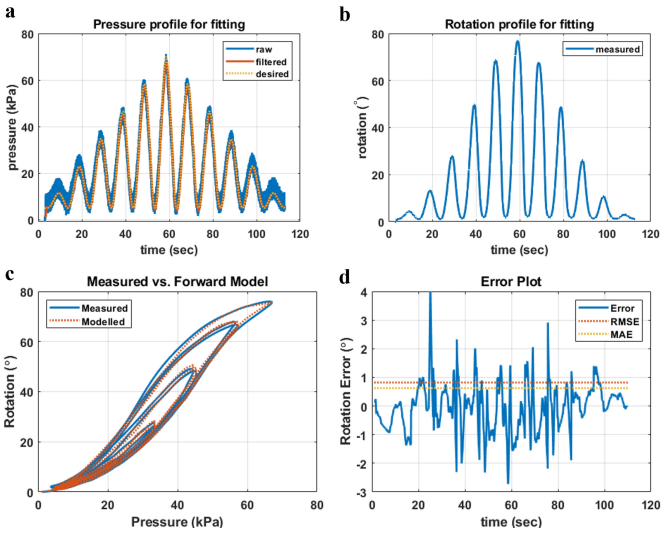

Fig. 2. Hysteresis model identification and validation results. (a) Input pressure profile used for model fitting, showing desired, raw, and filtered signals over time. (b) Corresponding measured rotational response of the actuator. (c) Comparison of the measured pressure-rotation hysteresis loop and the loop predicted by the fitted forward model. (d) Modeling error between the measured and predicted rotation, with the calculated Root Mean Square Error (RMSE) and Mean Absolute Error (MAE) shown as dotted lines.

via an Abaqus FEM simulation and a linear model was fitted to the calculated data:

$$V_a = K_{l1} l + K_{l0} \tag{10}$$

where $[K_{l1}, K_{l0}] = [0.0362, -1.6307]$.

The required rate of volume change, $\dot{V}_a$, is obtained by differentiating this equation. However, this process amplifies sensor noise. To address this, the noise component δ_l is explicitly incorporated into the modeling as follows.

$$\dot{V}_a = K_{l1}(\frac{dl}{dt} + \delta_l) \tag{11}$$

where $|\delta_l| \leq^{\exists} \delta_{l,max}$

D. Adaptive Robust Control

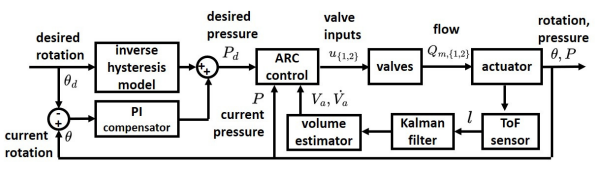

Fig. 3. Schematic diagram of the proposed ARC framework. Desired rotation (θ_d) is fed into an inverse hysteresis model to generate a feedforward desired pressure (P_d). A PI compensator corrects for rotational tracking error. The ARC controller computes the valve inputs ($u_{\{1,2\}}$) based on the pressure error and the estimated volume (V_a) and its rate of change ($\dot{V}_a$), which are derived from a ToF sensor and a Kalman filter.

The control configuration, illustrated in Fig. 3, employs a feedforward pressure command from the inverse hysteresis model, which is then corrected by a PI compensator. The core ARC strategy addresses two main uncertainties: the variation in valve conductance parameters and the measurement noise from the internal volume sensor. Experimental characterization of the valve confirmed a single linear model's insufficiency, validating our approach of treating conductance parameters as bounded variables.

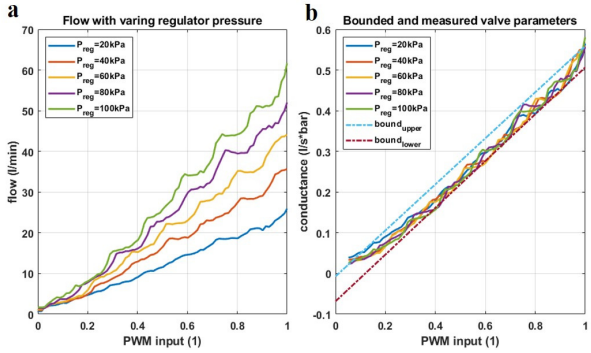

Fig. 4. Experimental characterization of the on-off valve used for pneumatic control. (a) Measured mass flow rate as a function of the PWM input for various upstream regulator pressures (P_{reg}). (b) Calculated sonic conductance derived from the flow data, showing the determined upper and lower bounds that are used for the adaptive robust controller design.

To model and control the estimation of these parameters, the following formulation is introduced. Let $\boldsymbol{\gamma} = [\gamma_1, \gamma_2] = [K_{c1}, K_{c0}]$, which satisfies:

$$\gamma \in \Omega_\gamma := \{\gamma : \gamma_{min} \leq \gamma \leq \gamma_{max}\}. \tag{12}$$

It can be considered that each parameter corresponding to $\boldsymbol{\gamma_{min}} = [\gamma_{1,min}, \gamma_{2,min}] = [K_{c1,min}, K_{c0,min}] = [0.5661, 0.0073]$, $\boldsymbol{\gamma_{max}} = [\gamma_{1,max}, \gamma_{2,max}] = [K_{c1,max}, K_{c0,max}] = [0.5750, 0.0684]$ can be modeled. A discontinuous projection mapping, $Proj$, is introduced to estimate $\boldsymbol{\gamma}$ with notation $\hat{\diamond}$ denoting estimating of $\diamond$.

$$\dot{\hat{\boldsymbol{\gamma}}} = Proj_{\hat{\boldsymbol{\gamma}}}(\boldsymbol{\Gamma\tau}), \tag{13}$$

$$Proj_{\hat{\boldsymbol{\gamma}}}(\diamond) = \begin{cases} 0, & \text{if } \hat{\gamma}_j = \gamma_{j,max} \wedge \diamond > 0 \\ 0, & \text{if } \hat{\gamma}_j = \gamma_{j,min} \wedge \diamond < 0 \\ \diamond, & \text{otherwise.} \end{cases} \tag{14}$$

where $\boldsymbol{\Gamma}$ is positive definite matrix. And the following properties are satisfied with any adaptation fuction τ.

$$\hat{\gamma} \in \Omega_\gamma := \{\gamma : \gamma_{min} \leq \gamma \leq \gamma_{max}\} \tag{15a}$$

$$\tilde{\boldsymbol{\gamma}}\,[\Gamma^{-1} Proj_{\hat{\boldsymbol{\gamma}}}(\Gamma\tau) - \tau] \leq 0, \,^{\forall}\tau. \tag{15b}$$

As shown in Fig.3, the desired pressure and its derivative required to achieve the target rotational value are calculated as follows.

IEEE Robotics and Automation Letters (RA-L) paper, presented at ICRA 2026, Vienna, Austria. Cite as RA-L paper.

$$P_d = \Psi^{-1}(x_1, \boldsymbol{y_0'}, t) + K_p(x_1 - x_{1d}) + K_i \int (x_1 - x_{1d})dt \tag{16a}$$

$$\dot{P}_d = \frac{d\Psi^{-1}(x_1, \boldsymbol{y_0'}, t)}{dt} + K_p(x_2 - x_{2d}) + K_i(x_1 - x_{1d}) \tag{16b}$$

where $[x_1, x_2]^T = [\theta, \dot{\theta}]^T$ is state vector, $[x_{1d}, x_{2d}]^T = [\theta_d, \dot{\theta_d}]^T$ is desired state, $\boldsymbol{y_0'}$ is set to $\mathbf{0}$ indicating initial condition, and K_p, K_i are proportional and integral gain to be selected to reduce the discrepency between real and modeled actuator behavior. The error dynamics with $S = P_a - P_d$ can be constructed as follow.

$$\dot{S} = \begin{cases} K_{u_1}(\gamma_1 u_1 - \gamma_2) - K_v(\frac{dl}{dt} + \delta_l) - \dot{P}_d, & 0 \le u_1 \le 1 \\ -K_{u_2}(\gamma_1 u_2 - \gamma_2) - K_v(\frac{dl}{dt} + \delta_l) - \dot{P}_d, & 0 \le u_2 \le 1 \end{cases} \tag{17}$$

where $K_{u1} = \frac{\rho_0 k R T_0}{V_a}\{P_{reg} f(P_{reg}, P_a, \sigma_{cr})\}$, $K_{u2} = \frac{\rho_0 k R T_0}{V_a}\{P_a f(P_a, P_{atm}, \sigma_{cr})\}$, $K_v = \frac{k P_a K_{l1}}{V_a}$ and $\gamma_{1,2}$ represents uncertain parameter of the valve's sonic conductance with bound of $(\gamma_{j,min}, \gamma_{j,max})$ for $j = 1, 2$. The ARC control inputs for the dynamics of the corresponding S could be configured as follows with an estimate of γ_j denoting $\hat{\gamma_j}$ for $j = 1, 2$ when the only valve 1 is operated.

$$u_1 = u_{1f} + u_{1s1} + u_{1s2} \tag{18a}$$

$$u_{1f} = (K_{u1}\hat{\gamma_1})^{-1}\{K_{u1}\hat{\gamma_2} + K_v\frac{dl}{dt} + \frac{d\Psi^{-1}(x_1)}{dt} + K_p(x_2 - x_{2d}) + K_i(x_1 - x_{1d})\} \tag{18b}$$

$$u_{1s1} = -(K_{u1}\gamma_{1,min})^{-1}KS \tag{18c}$$

$$u_{1s2} = -(K_{u1}\gamma_{1,min})^{-1}\frac{h_1^2 S}{4\epsilon} \tag{18d}$$

where ϵ and K are positive parameters that should be selected, and robustness function, h_1, is

$$h_1 = \Sigma_j\{\|\psi_1(j)\|(\gamma_{j,max} - \gamma_{j,min})\} + K_v\delta_{l,max} \tag{19}$$

where $\boldsymbol{\psi_1} = [K_{u1}u_{1f}, -K_{u1}]^T$, and $\delta_{l,max}$ is maximum value of δ_l. The adaptation function and update rule for updating parameter γ_j are as follows:

$$\boldsymbol{\tau_1} = \boldsymbol{\psi_1} S \tag{20a}$$

$$\dot{\hat{\boldsymbol{\gamma}}} = Proj_{\hat{\gamma}}(\boldsymbol{\Gamma\tau_1}) \tag{20b}$$

where $\boldsymbol{\Gamma} = [\Gamma_1 0; 0\Gamma_2]$. In the same way, the dynamics can be interpreted when the only valve 2 turn on as follows.

$$u_2 = u_{2f} + u_{2s1} + u_{2s2} \tag{21a}$$

$$u_{2f} = (K_{u2}\hat{\gamma_1})^{-1} - \{K_{u2}\hat{\gamma_2} - K_v\frac{dl}{dt} - \frac{d\Psi^{-1}(x_1)}{dt} - K_p(x_2 - x_{2d}) - K_i(x_1 - x_{1d})\} \tag{21b}$$

$$u_{2s1} = (K_{u2}\gamma_{1,min})^{-1}KS \tag{21c}$$

$$u_{2s2} = (K_{u2}\gamma_{1,min})^{-1}\frac{h_2^2 S}{4\epsilon} \tag{21d}$$

with

$$h_2 = \Sigma_j^b\{\|\psi_2(j)\|(\gamma_{j,max} - \gamma_{j,min})\} + K_v\delta_{l,max} \tag{22a}$$

$$\boldsymbol{\psi_2} = [-K_{u2}u_{2f}, K_{u2}]^T \tag{22b}$$

$$\boldsymbol{\tau_2} = \boldsymbol{\psi_2} S \tag{22c}$$

$$\dot{\hat{\boldsymbol{\gamma}}} = Proj_{\hat{\gamma}}(\boldsymbol{\Gamma\tau_2}). \tag{22d}$$

Using the ARC control input $u_{1,2}$ described above, the derivative of the Lyapunov function defined as $V_1 = \frac{1}{2}S^2$ is given the next inequalities.

$$\dot{V}_1 \le -\frac{\gamma}{\gamma_{min}}KS^2 + \epsilon \tag{23a}$$

$$V_1(t) \le V_1(0)e^{-2Kt} + \frac{\epsilon}{2K}(1 - e^{-2Kt}). \tag{23b}$$

In addition, the positive definite function defined by $V_2 = V_1 + \frac{1}{2}\tilde{\boldsymbol{\gamma}}\boldsymbol{\Gamma}^{-1}\tilde{\boldsymbol{\gamma}}$ can also be guaranteed convergence of estimated parameters by establishing the following inequalities:

$$\dot{V}_2 = \begin{cases} -\frac{\gamma_1}{\gamma_{1,min}}(\frac{h_1^2}{4\epsilon} + K)S^2 \le 0, & 0 \le u_1 \le 1 \\ -\frac{\gamma_1}{\gamma_{1,min}}(\frac{h_2^2}{4\epsilon} + K)S^2 \le 0, & 0 \le u_2 \le 1. \end{cases} \tag{24}$$

The detailed derivation for these stability results is presented in Appendix C.

IV. Results

A. Experimental setup

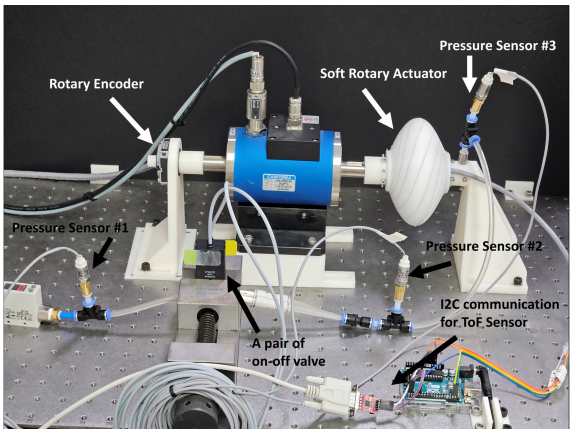

Fig. 5. Experimental setup for the soft rotary actuator system. The setup includes the soft rotary actuator, a rotary encoder for angle measurement, a pair of high-speed on-off valves for pneumatic control, and pressure sensors to monitor system pressures.

The experimental setup, illustrated in Fig.5, consists of the soft rotary actuator, a rotary encoder (AMT332S-V) for angle measurement, and a pair of high-speed on-off valves (MHJ10-S-2,5-QS-6-HF) for pneumatic control. A regulator (ITV2010-312N) supplies pneumatic flow, while three pressure sensors (PSE532-M5) monitor system pressures. A time-of-flight sensor (VL531X) is used to estimate the internal volume. Sensor data are transmitted to a compactRIO cDAQ-9178 via an Arduino Uno R3 for control processing.

The experiments were conducted under two distinct scenarios to rigorously evaluate the performance of our proposed

IEEE Robotics and Automation Letters (RA-L) paper, presented at ICRA 2026, Vienna, Austria. Cite as RA-L paper.

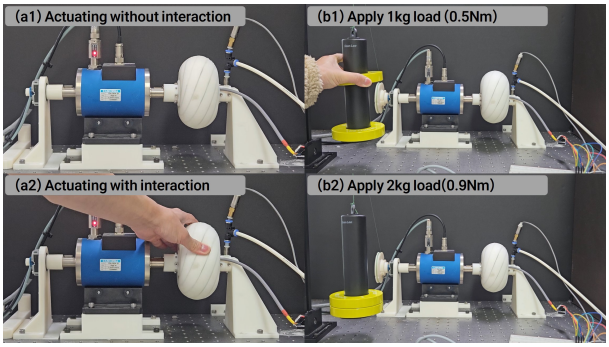

Fig. 6. Visual depiction of the experimental setups for Scenario A and Scenario B. Scenario A (Sensor Disturbance): (a1) Baseline actuation without physical interaction; (a2) Manual interaction by deforming the actuator to introduce sensor disturbances. Scenario B (External Load): (b1) Application of a 1 kg mass, resulting in a 0.5 Nm external torque; (b2) Application of a 2 kg mass, resulting in a 0.9 Nm external torque.

variable-volume model against the fixed-volume model. Scenario A focused on the controller's robustness against significant sensor disturbances, which were artificially introduced by repeatedly touching the ToF sensor's measurement path. Scenario B, conversely, tested the system's ability to handle external load variations, where a sudden increase in torque was applied using a cable and pulley system.

B. Experimental results

This section analyzes the experimental results to evaluate the performance of the proposed controller under two distinct modeling paradigms: the fixed-volume model and the variable-volume model.

1) Performance under Sensor Disturbance (Scenario A): In the initial baseline test (scenario a1), both the fixed-volume and variable-volume models demonstrated nearly indistinguishable rotation tracking quality, with comparable RMSE values as shown in Table I. A key distinction, however, was the control effort. The PWM input for the fixed-volume model was visibly more oscillatory, with an RMS value of 0.318, whereas the variable-volume model's RMS value was 0.238—a substantial 25.2% reduction. This indicates that our volume-aware approach achieves similar tracking performance with significantly more efficient and smoother control.

TABLE I
PERFORMANCE METRICS FOR EACH SCENARIOS.

scenario	θ_M	θ_R	P_M	P_R	u_M	u_R
a1:fixed	.709	.997	.649	.703	.248	.318
a2:fixed	.948	1.16	1.09	1.35	.371	.465
a1:variable	1.05	1.38	.618	.700	.201	.238
a2:variable	.872	1.04	.817	1.02	.291	.364
b1:fixed	.971	1.10	.672	.873	.361	.418
b2:fixed	.987	1.13	.877	1.16	.415	.468
b1:variable	.829	1.12	.487	.574	.215	.248
b2:variable	.945	1.06	.581	.667	.172	.231

Notes: θ_M and θ_R refer to MAE and RMSE of rotation in degrees, P_M and P_R refer to MAE and RMSE of pressure in kPa, u_M and u_R refer to MA and RMS of PWM input.

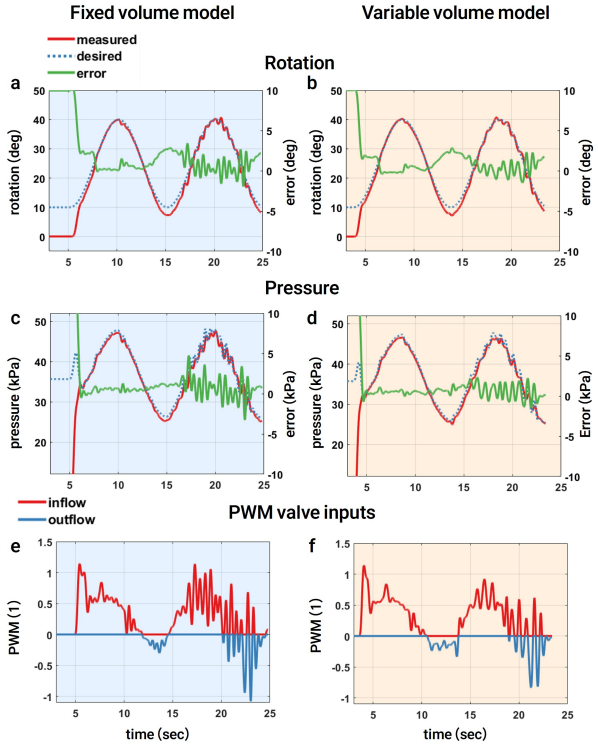

Fig. 7. Experimental results for Scenario A (Sensor Disturbance), comparing the fixed-volume model (left column, blue background) and the variable-volume model (right column, orange background). The first operational cycle corresponds to the baseline condition (a1), while the second cycle shows the system's response to the manual sensor disturbance (a2). (a), (b) Rotation tracking performance, showing measured (solid red), desired (dotted blue), and error (solid green) signals. (c), (d) Corresponding pressure tracking performance. (e), (f) PWM valve inputs required by each model.

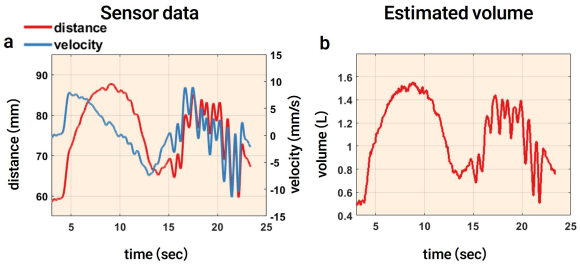

Fig. 8. Effect of the manual physical disturbance applied during scenario a2. (a) Raw data from the time-of-flight sensor, showing the measured internal distance and its calculated velocity. High-frequency oscillations are visible during the disturbance period. (b) The resulting estimated internal volume of the actuator, which is corrupted by the noisy sensor data from (a).

The second phase of the experiment (scenario a2) introduced a direct physical disturbance to the ToF sensor, successfully corrupting its distance measurements as shown in Fig. 8(a). Despite this direct data corruption, both models maintained robust tracking without failure, as seen in the second cycle of Fig. 7. Notably, the variable-volume model demonstrated superior robustness; its rotation tracking RMSE

IEEE Robotics and Automation Letters (RA-L) paper, presented at ICRA 2026, Vienna, Austria. Cite as RA-L paper.

improved from 1.38 in scenario a1 to 1.04 in scenario a2, while the fixed-volume model's error increased. As expected, both controllers reacted to the disturbance with more aggressive PWM inputs, reflected by the increased RMS values in Table I for scenario a2.

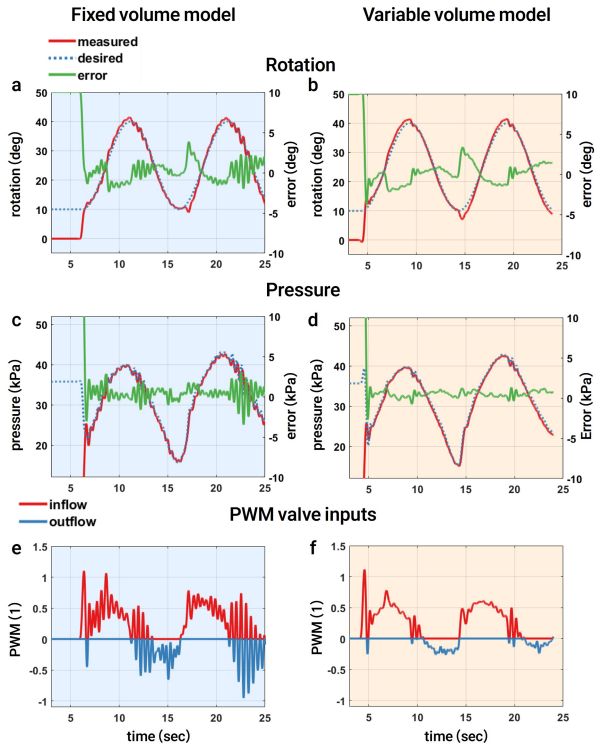

Fig. 9. Experimental results for Scenario B (External Load Variation), comparing the fixed-volume model (left column) and the variable-volume model (right column). The first operational cycle shows the system response under a 0.5 Nm external torque (b1), while the second cycle shows the response to an increased torque of 0.9 Nm (b2). (a), (b) Rotation tracking performance. (c), (d) Corresponding pressure tracking. (e), (f) PWM valve inputs required by each model.

2) Performance under External Load Variation (Scenario B): This scenario evaluated the controller's robustness against an abrupt increase in external load from 0.5 Nm to 0.9 Nm. Despite this significant disturbance, both the fixed-volume and variable-volume models maintained effective trajectory tracking without failure, as visually confirmed in Fig. 9(a,b). However, a critical distinction emerged in the control effort required. The fixed-volume model necessitated a markedly more oscillatory and aggressive PWM input to compensate for the external torque. In stark contrast, the proposed variable-volume model maintained a significantly smoother and more moderate control action. Quantitatively, the variable-volume model achieved robust tracking with a 50.6% reduction in PWM input RMS value compared to the fixed-volume model under the 0.9 Nm load, indicating substantially greater efficiency and stability.

V. Discussion

Accurate system modeling is critical for robust, energy-efficient control of soft pneumatic actuators. While both fixed- and variable-volume models tracked trajectories successfully under disturbances, the latter proved more efficient against external loads. The fixed-volume model required aggressive inputs for compensation, whereas the proposed approach achieved equal performance with substantially reduced effort—specifically, a 50.6% energy reduction under a 0.9 Nm load. This confirms that ARC frameworks achieve superior efficiency without sacrificing robustness only by explicitly incorporating the actuator's volume dynamics.

Appendix

Nomenclature

Pneumatic and Valve Dynamics	
P_{reg}, P_{atm}	Regulator and atmospheric pressures
P_u, P_d	Upstream and downstream pressures of a valve
P, V_a	Actuator internal pressure and volume
Q_m	Mass flow rate through a valve
C	Sonic conductance of a valve
σ_{cr}	Critical pressure ratio of a valve
u_1, u_2	PWM control inputs for inflow and outflow valves
K_{c1}, K_{c0}	Coefficients for the valve conductance model
k, R	Specific heat ratio and gas constant of air
Hysteresis Model (MPI)	
Ψ, Ψ^{-1}	Forward and inverse MPI hysteresis models
H_r, D_d	Play and deadzone operators
$\boldsymbol{r_h}, \boldsymbol{d}$	Threshold vectors for play and deadzone operators
$\boldsymbol{w_h}, \boldsymbol{w_d}$	Weight vectors for play and deadzone operators
Volume Estimation	
l	Internal distance measured by the ToF sensor
K_{l1}, K_{l0}	Coefficients for the linear volume estimation model
$\delta_l, \delta_{l,max}$	Bounded noise and its maximum value for the ToF sensor measurement
Adaptive Robust Control (ARC)	
$\theta, \dot{\theta}$	Actuator rotation angle and angular velocity
$\theta_d, \dot{\theta_d}$	Desired rotation angle and angular velocity
K_p, K_i	Gains for the outer-loop PI compensator
S	Pressure tracking error $(P - P_d)$
$\boldsymbol{\gamma}$	Vector of uncertain valve parameters, $[K_{c1}, K_{c0}]^T$
$\hat{\boldsymbol{\gamma}}, \tilde{\boldsymbol{\gamma}}$	Estimated and error vectors of $\boldsymbol{\gamma}$
$\boldsymbol{\gamma_{min}}, \boldsymbol{\gamma_{max}}$	Lower and upper bounds of $\boldsymbol{\gamma}$
u_f, u_{s1}, u_{s2}	Feedforward, stabilizing, and robust control terms
K, ϵ	Positive gains for the linear stabilizing and robust terms
h_1, h_2	Robustness functions for inflow and outflow control
$\boldsymbol{\psi_1}, \boldsymbol{\psi_2}$	Regression vectors for parameter adaptation
$\boldsymbol{\tau_1}, \boldsymbol{\tau_2}$	Adaptation functions
$\boldsymbol{\Gamma}$	Adaptation gain matrix
V_1, V_2	Lyapunov function candidates

A. Parameters of Inverse Modified Prandtl-Ishlinskii Model

The parameters for the inverse Modified Prandtl-Ishlinskii (MPI) model, essential for the feedforward control path, are computed directly from the forward model parameters $(\boldsymbol{w_h}, \boldsymbol{r_h}, \boldsymbol{w_d}, \boldsymbol{d})$ which were identified experimentally and are listed in Appendix B. The inverse model Ψ^{-1} is used to calculate the desired pressure required to achieve a target rotation.

IEEE Robotics and Automation Letters (RA-L) paper, presented at ICRA 2026, Vienna, Austria. Cite as RA-L paper.

$$w'_{h_0} = 1/w_{h_0} \tag{25a}$$
$$w'_{h_i} = -\frac{w_{h_i}}{\left(\sum_{j=0}^{i} w_{h_j}\right)\left(\sum_{j=0}^{i-1} w_{h_j}\right)}, \quad i = 1\dots n \tag{25b}$$
$$r'_i = \sum_{j=0}^{i} w_{h_j}(r_i - r_j) \tag{25c}$$
$$y'_{0_i} = \sum_{j=0}^{i} w_{h_j} y_{0_j}, \qquad i = 1\dots n \tag{25d}$$
$$w'_{d_0} = 1/w_{d_0} \tag{25e}$$
$$w'_{d_i} = -\frac{w_{d_i}}{\left(\sum_{j=0}^{i} w_{d_j}\right)\left(\sum_{j=0}^{i-1} w_{s_j}\right)}, \quad i = 1\dots m \tag{25f}$$
$$d'_i = \sum_{j=0}^{i} w_{d_j}(d_i - d_j), \qquad i = 0\dots m. \tag{25g}$$

B. Parameters Fitted for MPI Model

The optimized parameters for the forward Modified Prandtl-Ishlinskii (MPI) model are summarized in this table. These parameters, which characterize the hysteresis loop between the actuator's internal pressure and rotational angle, were identified by minimizing the Root Mean Square Error (RMSE) using the experimental data shown in Fig. 2.

C. Detailed Stability Analysis

This appendix provides the detailed mathematical derivations for the stability of the proposed ARC framework, leading to the results presented in (23) and (24). The analysis is presented for the case where valve 1 is active; the procedure for valve 2 is analogous.

1) Boundedness of Tracking Error (Analysis of V_1): First, we demonstrate the uniform ultimate boundedness (UUB) of the tracking error S by analyzing the Lyapunov function $V_1 = \frac{1}{2}S^2$. After substituting the control law (18) into the system dynamics (17), the time derivative of V_1 can be expressed as:

$$\dot{V}_1 = S[K_{u1}\gamma_1 u_{1s2} - (\boldsymbol{\psi_1}^T\tilde{\boldsymbol{\gamma}} - K_v\delta_l)] - \frac{\gamma_1}{\gamma_{1,min}}KS^2 \tag{26a}$$
$$= -\frac{\gamma_1}{\gamma_{1,min}}\frac{h_1^2 S^2}{4\epsilon} + S(\boldsymbol{\psi_1}^T\tilde{\boldsymbol{\gamma}} - K_v\delta_l) - \frac{\gamma_1}{\gamma_{1,min}}KS^2 \tag{26b}$$

where the robustness function h_1 from (19) is defined to satisfy the property $|\boldsymbol{\psi_1}^T\tilde{\boldsymbol{\gamma}} - K_v\delta_l| \le h_1$. By using the inequality $|S|h_1 \le \frac{h_1^2 S^2}{4\epsilon} + \epsilon$, we can bound the uncertainty terms. This leads to the final inequality for $\dot{V}_1$ as presented in (23):

$$\dot{V}_1 \le -\frac{\gamma_1}{\gamma_{1,min}}KS^2 + \epsilon \tag{27}$$

which can be rewritten as $\dot{V}_1 \le -2(\frac{\gamma_1}{\gamma_{1,min}}K)V_1 + \epsilon$. This result guarantees that the tracking error S is uniformly ultimately bounded, converging to a small set whose size is determined by the design parameter ϵ.

2) Asymptotic Stability of Tracking Error (Analysis of V_2): To prove the stability of the overall system including parameter estimation, we analyze the composite Lyapunov function $V_2 = V_1 + \frac{1}{2}\tilde{\boldsymbol{\gamma}}^T\boldsymbol{\Gamma}^{-1}\tilde{\boldsymbol{\gamma}}$. The time derivative of V_2, using the property of the projection mapping from (15) and the adaptation law from (20), satisfies:

$$\dot{V}_2 = \dot{V}_1 + \tilde{\boldsymbol{\gamma}}^T\boldsymbol{\Gamma}^{-1}\dot{\tilde{\boldsymbol{\gamma}}} = \dot{V}_1 - \tilde{\boldsymbol{\gamma}}^T\boldsymbol{\Gamma}^{-1}\dot{\hat{\boldsymbol{\gamma}}}$$
$$\le \dot{V}_1 - \tilde{\boldsymbol{\gamma}}^T\boldsymbol{\tau_1} = \dot{V}_1 - \tilde{\boldsymbol{\gamma}}^T\boldsymbol{\psi_1}S \tag{28a}$$

Here, the term $K_v\delta_l$ is incorporated into the adaptation law through the robustness function h_1. Substituting the expression for $\dot{V}_1$ from (26a):

$$\dot{V}_2 \le \left[S(K_{u1}\gamma_1 u_{1s2}) + S(\boldsymbol{\psi_1}^T\tilde{\boldsymbol{\gamma}}) - S(K_v\delta_l) - \frac{\gamma_1}{\gamma_{1,min}}KS^2\right]$$
$$- \boldsymbol{\psi_1}^T\tilde{\boldsymbol{\gamma}}S \tag{29a}$$
$$= S(K_{u1}\gamma_1 u_{1s2}) - S(K_v\delta_l) - \frac{\gamma_1}{\gamma_{1,min}}KS^2 \tag{29b}$$

The robust control term u_{1s2} is designed to handle all bounded uncertainties. As a result, the uncertainty terms perfectly cancel out, yielding the final expression as shown in (24):

$$\dot{V}_2 = -\frac{\gamma_1}{\gamma_{1,min}}\left(\frac{h_1^2}{4\epsilon} + K\right)S^2 \le 0 \tag{30}$$

Since $\dot{V}_2 \le 0$, V_2 is non-increasing and bounded. This ensures that S is bounded and, by applying Barbalat's Lemma, it can be concluded that $S \to 0$ as $t \to \infty$, confirming the asymptotic stability of the tracking error.

TABLE II
MPI PARAMETERS OPTIMIZED BY MINIMIZING RMSE

i	0	1	2	3	4
r_h	0	0.3478	0.5160	1.143	2.072
w_h	0.05	0.696	0.999	0.122	0.0125
d	0	14.21	27.122	28.00	38.28
w_d	0.062	0.195	0.394	0.050	0.050
i	5	6	7	8	9
r_h	3.074	5.573	10.10	22.38	36.84
w_h	0.292	0.050	0.050	0.050	0.100
d	38.35	45.16	45.17	45.17	46.52
w_d	0.050	0.050	0.050	0.050	0.050

D. Common Control Parameters

The following parameters were held constant across all scenarios to ensure a consistent comparison between the different test conditions and modeling approaches. The sonic conductance bounds were set as $\gamma_1 \in [0.5661, 0.5750]$ and $\gamma_2 \in [0.0073, 0.0684]$. The PI and ARC controller gains were set as $K_s = 15$, $K_p = 1.5$, $K_i = 1.5$, with a maximum PWM input of $P_{sup} = 1.0$. The inverse hysteresis model's gain was set to $K_c = 20$, and the adaptation gain was $\Gamma = 10$.

REFERENCES

[1] Z. Chen, D. Wu, Q. Guan, D. Hardman, F. Renda, J. Hughes, T. G. Thuruthel, C. D. Santina, B. Mazzolai, H. Zhao, and C. Stefanini, "A Survey on Soft Robot Adaptability: Implementations, Applications, and Prospects [Survey]," *IEEE Robotics & Automation Magazine*, pp. 2–14, 2025.

[2] A. P. Sabelhaus, Z. J. Patterson, A. T. Wertz, and C. Majidi, "Safe Supervisory Control of Soft Robot Actuators," *Soft Robotics*, vol. 11, no. 4, pp. 561–572, Aug. 2024.

[3] Z. Gao, Z. Liao, and C. Li, "Better interaction experience: Human-machine interface for soft robotic systems," *Intelligence & Robotics*, vol. 5, no. 3, pp. 520–40, June 2025.

[4] N. Ghobadi, W. Kinsner, T. Szturm, and N. Sepehri, "Design and Evaluation of a Soft Robotic Actuator with Non-Intrusive Vision-Based Bending Measurement," *Sensors*, vol. 25, no. 13, p. 3858, June 2025.

[5] H. Ma, J. Zhou, C.-H. Yeow, and L. Meng, "State Estimation by Joint Approach With Dynamic Modeling and Observer for Soft Actuator," *IEEE Robotics and Automation Letters*, vol. 9, no. 12, pp. 11 706–11 713, Dec. 2024.

[6] Y. Liu, D. Zhang, Y. Yu, P. Chen, W. Shi, and D. Wang, "Position control of a soft pneumatic actuator based on the pressure parameter feedback model (PPFM)," *Mechanical Sciences*, vol. 15, no. 2, pp. 407–416, July 2024.

[7] M. N. M. Nasir, I. N. A. M. Nordin, A. A. M. Faudzi, M. N. Muftah, M. A. M. Yusoff, and S. Mohamaddan, "Modeling and Position Control of Fiber Braided Bending Actuator Using Embedded System," *Applied Sciences*, vol. 13, no. 5, p. 3170, Mar. 2023.

[8] Q. Yang and Z. Liu, "Model-based versus model-free optimal tracking for soft robots: Analytical and data-driven Koopman modeling, control design and experimental validation," *Nonlinear Dynamics*, vol. 112, no. 17, pp. 15 267–15 287, Sept. 2024.

[9] E. H. Skorina, M. Luo, S. Ozel, F. Chen, W. Tao, and C. D. Onal, "Feedforward augmented sliding mode motion control of antagonistic soft pneumatic actuators," in *2015 IEEE International Conference on Robotics and Automation (ICRA)*. Seattle, WA, USA: IEEE, May 2015, pp. 2544–2549.

[10] J. De La Morena, F. Ramos, and A. S. Vázquez, "Hysteresis Modeling of Soft Pneumatic Actuators: An Experimental Review," *Actuators*, vol. 14, no. 7, p. 321, June 2025.

[11] Y. Hu, C. Chen, and J. Zou, "Model-Based Contact Detection and Accommodation for Soft Bending Actuators: An Integrated Direct/Indirect Adaptive Robust Approach," *IEEE Robotics and Automation Letters*, vol. 7, no. 3, pp. 7263–7270, July 2022.

[12] H. T. M. Nu, L. Q. Viet, and L. T. Truyen, "A sensorless soft pneumatically powered actuator," *Proceedings of the Institution of Mechanical Engineers, Part C: Journal of Mechanical Engineering Science*, vol. 239, no. 15, pp. 5941–5960, Aug. 2025.

[13] S. Zhao, Z. Yan, Q. Meng, H. Xiao, X. Lai, and M. Wu, "Modified Three-Element Modeling and Robust Tracking Control for a Planar Pneumatic Soft Actuator," *IEEE Transactions on Industrial Electronics*, vol. 70, no. 9, pp. 9237–9247, Sept. 2023.

[14] C. Chen and J. Zou, "Adaptive robust control of soft bending actuators: An empirical nonlinear model-based approach," *Journal of Zhejiang University-SCIENCE A*, vol. 22, no. 9, pp. 681–694, Sept. 2021.

[15] K. Li, T. Nuchkrua, H. Zhao, Y. Yuan, and S. Boonto, "Learning-based Adaptive Robust Control of Manipulated Pneumatic Artificial Muscle Driven by H_2 -based Metal Hydride," in *2018 IEEE 14th International Conference on Automation Science and Engineering (CASE)*. Munich, Germany: IEEE, Aug. 2018, pp. 1284–1289.

[16] T. R. Young, Y. K. Yong, and A. J. Fleming, "Data-Driven Inverse Control of Pneumatic Soft Robotic Actuators with On-Off Valves: Simulated Performance," in *2025 IEEE International Conference on Mechatronics (ICM)*. Wollongong, Australia: IEEE, Feb. 2025, pp. 1–7.

[17] M. S. Xavier, A. J. Fleming, and Y. K. Yong, "Nonlinear Estimation and Control of Bending Soft Pneumatic Actuators Using Feedback Linearization and UKF," *IEEE/ASME Transactions on Mechatronics*, vol. 27, no. 4, pp. 1919–1927, Aug. 2022.

[18] C. Chen, W. Tang, Y. Hu, Y. Lin, and J. Zou, "Fiber-reinforced soft bending actuator control utilizing on/off valves," *IEEE Robotics and Automation Letters*, vol. 5, no. 4, pp. 6732–6739, 2020.

[19] S. Joshi and J. Paik, "Pneumatic Supply System Parameter Optimization for Soft Actuators," *Soft Robotics*, vol. 8, no. 2, pp. 152–163, Apr. 2021.

[20] J. Poccard-Saudart, S. Xu, C. B. Teeple, N.-S. P. Hyun, K. P. Becker, and R. J. Wood, "Controlling Soft Fluidic Actuators Using Soft DEA-Based Valves," *IEEE Robotics and Automation Letters*, vol. 7, no. 4, pp. 8837–8844, Oct. 2022.

[21] P. Polygerinos, N. Correll, S. A. Morin, B. Mosadegh, C. D. Onal, K. Petersen, M. Cianchetti, M. T. Tolley, and R. F. Shepherd, "Soft robotics: Review of fluid-driven intrinsically soft devices; manufacturing, sensing, control, and applications in human-robot interaction," *Advanced Engineering Materials*, vol. 19, no. 12, p. 1700016, 2017.